Applied Acoustics 221 (2024) 110007

Contents lists available at ScienceDirect

Applied Acoustics

journal homepage: www.elsevier.com/locate/apacoust

Sound absorption in sonic black holes: Wave retarding effect with broadband cavity resonance

Xiaoqi Zhang [a], Nianwen He [a], Li Cheng [b], Xiang Yu [b], Linke Zhang [a,c,*], Fucai Hu [a,*]

[a] School of Naval Architecture, Ocean and Energy Power Engineering, Wuhan University of Technology, Wuhan 430063, China
[b] Department of Mechanical Engineering, The Hong Kong Polytechnic University, Kowloon, Hong Kong, China
[c] Key Laboratory of High Performance Ship Technology, Wuhan University of Technology, Wuhan 430063, China

ARTICLE INFO

Keywords:
Sonic black hole
Energy dissipation mechanism
Wave retarding
Broadband cavity resonance

ABSTRACT

Energy dissipation mechanism of Sonic black hole (SBH) structure with limited number of inner rings inside a duct has not been fully apprehended. On the top are the unclearly revealed dominant energy dissipation region, and inherent relationship among SBH induced wave retarding effect, cavity resonance and the final sound absorption to be achieved. To alleviate these problems, numerical analyses are conducted using finite element (FE) simulations with due consideration of the thermal-viscous losses in a SBH for sound absorption assessment and underlying sound absorption mechanism exploration. The validity of the FE model is confirmed through comparisons with experimental data acquired from impedance tube tests. Analyses first identify the vicinity of the inner ring wall as the predominant energy dissipation region, and the primary source of dissipation comes from the strong friction occurred through cavity resonance-induced high pressure gradient. Moreover, SBH induced wave retarding effect drastically changes the resonance behavior of individual cavity from conventional narrowband resonance with single resonant peak to broadband resonance with multiple resonant peaks, alongside the down-shifting of the resonant frequencies. Altogether, cascaded effects finally lead to the low frequency and broadband sound absorption. Studies presented in this work can provide guidelines for better SBH design in future.

1. Introduction

Acoustic Black Hole (ABH) stands out as a promising passive device for controlling noise and vibration by effectively trapping and absorbing waves through meticulous waveguide design. ABH effects feature a gradual reduction in the phase velocity of propagating waves to nearly zero, so that it takes infinite time theoretically for incoming waves to reach the boundary. Consequently, reflections from the boundary are nullified, thus generating effective energy trapping and dissipation when proper absorption is deployed [1–3]. This phenomenon draws an analogy to the concept of a “black hole” in astrophysics [4]. The remarkable wave deceleration and energy-trapping characteristics of the ABHs have received vast attention, particularly in the realm of passive structural vibration control [5–8].

While ABHs have predominantly been studied for manipulating bending waves in mechanical structures like beams or plates, research on Sonic Black Holes (SBHs) specifically tailored for sound wave manipulation remains limited, with only a handful of exploratory works [9–21]. The inaugural exploration in this domain was conducted by Mironov [9], in which the theoretical baseline of sound wave propagation in a one-dimensional waveguide with a varying cross-section and acoustic wall admittance was established to show the existence of the ABH effect in acoustics. In their work, the SBH was implemented by incorporating a substantial number of rings with a power-law-decaying inner radius into a duct. However, practical constraints limit the number of the inner rings, resulting in a discrete wave propagation boundary that deviates from the ideal continuously varying boundary impedance. Achieving a perfect ABH effect under practical conditions is therefore challenging. Nonetheless, references [10–12] experimentally showcased the potential of the SBH-based design for achieving remarkable sound reflection reduction using realistic SBH structures. To comprehensively characterize and analyze the acoustic properties of discrete SBH structures (with limited number of inner rings), various models [13–15,17] have been developed, with findings in line with experimental results. While the wave retarding phenomenon seems to be well investigated, energy dissipation alongside the underlying physics, however, remains

* Corresponding authors at: School of Naval Architecture, Ocean and Energy Power Engineering, Wuhan University of Technology, Wuhan 430063, China.
E-mail addresses: lincol@whut.edu.cn (L. Zhang), hufucai8@163.com (F. Hu).

https://doi.org/10.1016/j.apacoust.2024.110007
Received 5 December 2023; Received in revised form 23 March 2024; Accepted 31 March 2024
Available online 17 April 2024
0003-682X/© 2024 Elsevier Ltd. All rights reserved.

obscure. In fact, the wave trapping and energy dissipation mechanisms for practical SBHs might differ from the ideal scenario [9]. In this regard, it is imperative to know how the acoustic energy is dissipated in a practical discrete SBH structure. Recently, this topic attracted great attention from the literature [17–19]. Although the cavity resonance effect has been found to be related to the sound absorption, this effect alone cannot ensure broadband sound absorption due to the narrow band feature. Meanwhile, it was hypothesized that ABH-induced wave speed reduction could be independent from sound absorption [19], and the wave retarding effect actually has never been considered together with cavity resonance to explore the sound energy dissipation mechanism in a SBH. Therefore, the inherent relationship among SBH induced wave retarding effect, cavity resonance and sound absorption is yet to be elucidated.

Literature report the attempt of applying a small amount of sound absorbing material at the end of a SBH in views of achieving effects similar to its structural counterpart with damping layers [11,12]. However, this treatment was found to be ineffective, since the dominant energy dissipation areas were not clearly identified. The lack of understanding on the energy dissipation mechanism and dominant region are also the main reason why, in our previous work [20], the entire SBH boundary was treated with perforated panel, instead of a small amount of partial dissipation treatment. The identification of the dominant acoustic energy dissipation area was discussed in reference [18], where the absorption effects at the outer surface of the cylinder tube was identified as the main damping source.

In summary, despite the previous efforts, a thorough understanding of the sound absorption mechanism in a discrete SBH structure is still lacking. Most importantly, it is unclear how the SBH induced wave retarding effect, cavity resonance and sound absorption are inter-related and where the acoustic energy is predominantly dissipated. These issues motivate the present work. In this paper, a linear discrete SBH structure is investigated using a FE model, which considers viscous and thermal losses in a SBH. Numerical and experimental analyses are conducted to assess its sound absorption performance and to scrutinize the physical mechanisms behind.

The rest of the paper is organized as follows. The designed discrete SBH structure as well as the FE model used for analyses are first detailed in section 2. Analyses are then conducted in section 3 to scrutinize the physical mechanisms underpinning the sound absorption performance of the proposed structure. In section 4, experiments are carried out to validate the FE model, before main conclusions are summarized in section 5.

2. SBH model

2.1. Conceptual model

The SBH structure under investigation is shown in Fig. 1. It has an outer radius of $R = 30$ mm and a length of $L = 202$ mm. Within the structure, a total of 19 rings are installed, each with a wall thickness of 2 mm. The inner radii of these rings, $r(x)$, decrease linearly along the axis direction from the SBH inlet to its end, according to a linear relationship: $r(x) = R - \frac{R}{L}x$, where x denotes the position of the rings. Such a SBH structure is referred to as Linear Sonic Black Hole (LSBH). Numbered from the end of SBH, the distance separates the first ring from the SBH end is 10 mm. The remaining rings are equally spaced from each other at interval of 8 mm.

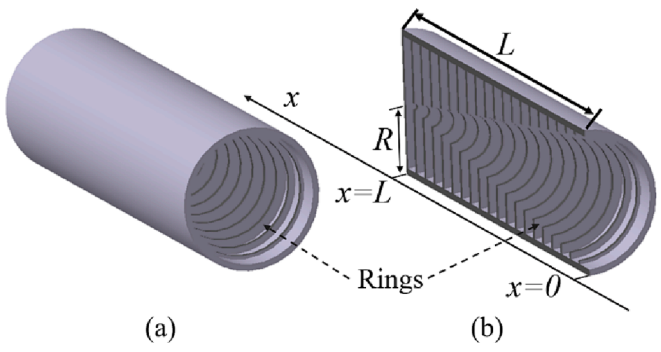

Fig. 1. Conceptual view of the SBH structure: (a) the overall structure; (b) detailed inner structure.

2.2. Analysis model

The LSBH device is to be installed as a termination in a circular duct of radius R, in which an incoming sound plane wave is fired from the inlet of the duct. FE method is adopted to evaluate the acoustic performance of the investigated device by using commercial software COMSOL, and Thermo-viscous Acoustics Interface was employed to account for viscosity and thermal dissipation within the acoustic boundary layer near the SBH inner walls by solving the linearized Navier–Stokes (LNS) equation, as described below [22].

$$i\omega\rho_1 + \nabla \bullet (\rho_0 \boldsymbol{u}_1) = 0$$

$$i\omega\rho_0 c_p T_1 - i\omega\alpha_p T_1 p_1 = \nabla \bullet (\kappa \nabla T)$$

$$i\omega\rho_0 \boldsymbol{u}_1 = \nabla \bullet (-p_1 J + \mu(\nabla \boldsymbol{u}_1 + (\boldsymbol{u}_1)^{\top}) - \left(\frac{2}{3}\mu - \mu_B\right)(\nabla \bullet \boldsymbol{u}_1)J)$$

$$c_p = (\frac{\partial \boldsymbol{u}_1}{\partial T})_p$$

$$\alpha_p = -\frac{1}{\rho}\left(\frac{\partial \rho}{\partial T}\right)_p \tag{1}$$

In the above set of equation, ∇ is the gradient operator, $\top$ denotes the transpose of a vector and the dependent variables encompass the air particle velocity vector $\mathbf{u}$, the pressure p, the temperature T, the density ρ and the angular frequency ω. Moreover, c_p is the specific heat at constant pressure (unit mass specific heat), α_p is the thermal expansion coefficient, κ is the thermal conductivity. Variables related to viscosity consist of μ for dynamic viscosity, and μ_B bulk viscosity. Finally, J represents the unit tensor. Subscripts 0 and 1 are used to denote the 0th-order background field and 1st-order acoustic perturbation, respectively.

Considering the axisymmetric nature of LSBH, two-dimensional (2D) model, as shown in Fig. 2(a), is adopted. In the contacting regions between air domains and solid walls, the size of the first mesh layer is set to be $\delta_{SBH}/5$ to ensure at least 5 mesh layers in the acoustic boundary layer region, where δ_{SBH} is the thickness of the acoustic boundary layer in SBH at the maximum frequency of interest. The conventional acoustic boundary layer thickness can be estimated by [23]

$$\delta = \sqrt{\frac{2\mu}{\rho_0 \omega}} \tag{2}$$

However, in light of the work in Ref. [14], the gradually decreased wave speed is actually equivalent to a gradual increase in the fluid density, which leads to a thinner acoustic boundary layer. As a result, the acoustic boundary layer in the SBH can be estimated by:

$$\frac{c_{SBH}}{c_0} = \frac{\delta_{SBH}}{\delta} \tag{3}$$

In the present case, using the maximum frequency of 1500 Hz and nominal air parameters, $\rho_0 = 1.29\ kg/m^3$ and $\mu = 1.8 \times 10\text{e-}5\ Pa{\cdot}s$, the conventional acoustic boundary layer thickness δ is around 0.055 mm. Considering the reduced sound speed in the SBH with $C_{SBH} = 59$ m/s at 1500 Hz, which is obtained through transient simulation presented later, yields $\delta_{SBH} \approx 0.01$ mm.

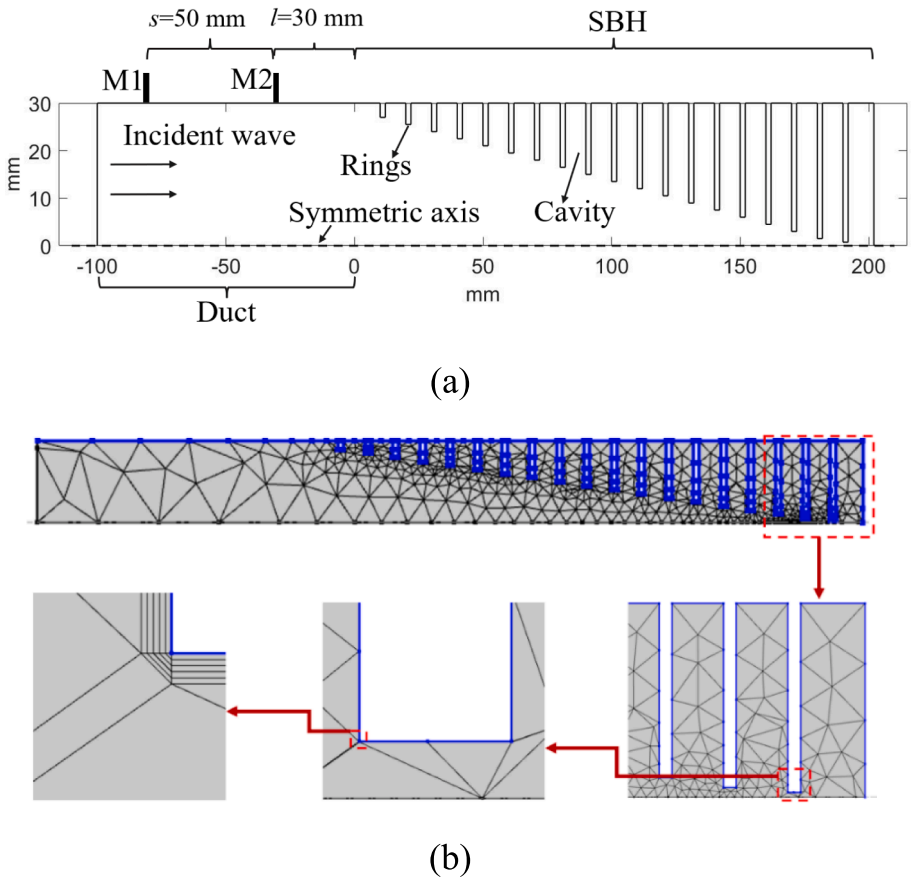

Fig. 2. (a) 2D axisymmetric model of the SBH; (b) discretized computational domain.

Beyond the acoustic boundary layer regions, the mesh is refined following the general acoustic simulation rule of ensuring a minimum of six elements per wavelength, in order to capture the fine details of the acoustic wave fluctuation and reduce the computation costs. The discretized computational domain is shown in Fig. 2 (b). The convergence of the solution in relation to meshing is conducted and the results indicate that convergence can be achieved to the accuracy needed for sound absorption prediction.

An incident acoustic plane wave of 1 Pa in amplitude is imposed on the inlet boundary of the duct. While ensuring a reasonable noise-to-signal ratio, the excitation level is set not to be extremely high. Alongside the much higher mechanical impedance of the metal ring (as compared to that of the air), rigid boundary condition can be applied to the wall and the inner rings of the SBH so that the coupling between sound wave and the structure can be neglected. To determine the sound absorption coefficient α, two-microphone transfer function method is employed, which can be described by the following set of equation.

$$H_{12} = \frac{p_{M2}}{p_{M1}}$$

$$r = \frac{H_{12} - e^{-jks}}{e^{jks} - H_{12}} e^{2jk(s+l)}$$

$$\alpha = 1 - |r|^2 \tag{4}$$

where H_{12} represents the sound pressure transfer function; p_{M1} and p_{M2} are the sound pressure at two points in the duct, *M1* and *M2*, respectively, which are separated by a distance *S* as shown in Fig. 2(a); *l* is the distance between *M2* and the entrance of SBH; *k* is the wave number; *r* is the reflection coefficient; *j* is the imaginary unit $j^2 = -1$.

The applicable frequency range for FE method analysis is constraint by the plane wave assumption, specified in Eq. (5) below and the distance between the two microphones *S* through Eq. (6):

$$f \le \frac{0.58 c_0}{D} \tag{5}$$

$$\frac{0.05 c_0}{S} \le f \le \frac{0.45 c_0}{S} \tag{6}$$

where *D* is the diameter of the duct, c_0 the sound speed in air.

3. Analyses and discussions

3.1. Sound absorption

The simulated sound absorption coefficient curve is presented in Fig. 3. It can be seen that the absorption coefficient initially undergoes a rapid ascent, reaching 0.92 at approximately 165 Hz, and then oscillates alongside the appearance of multiple peaks and dips in the curve. As the acoustic excitation frequency increases, the troughs gradually elevate, resulting in a smoother and more flattened absorption curve at higher frequencies. Notably, the 0.5 sound absorption bandwidth, defined as the frequency range corresponding to a sound absorption coefficient above 0.5, commences at a low frequency of 140 Hz. With $L = 202$ mm and the acoustic wavelength $\lambda = 2450$ mm at 140 Hz, the LSBH length is roughly $\lambda/12$, which makes it a subwavelength sound absorption device. Remarkably, the absorption coefficient exceeds 0.7 from 200 Hz and steadily approaches to 1 till the highest frequency of interest, demonstrating low frequency and broadband sound absorption. The acoustic performance of SBH can be affected by various parameters, including the position and number of inner rings, the profile of decreasing inner radii, the dissipation magnitudes and etc. A comprehensive exanimation

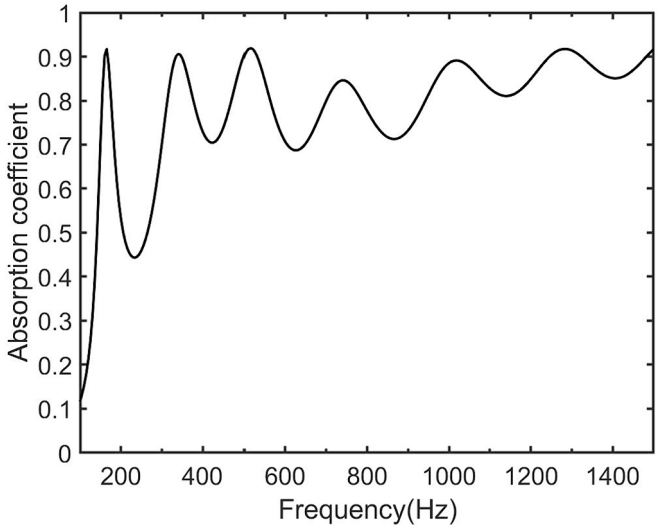

Fig. 3. Simulated sound absorption coefficient curve of the investigated LSBH.

of these parameters has been conducted and reported in Ref. [13]. Therefore, a detailed investigation into the influence of individual parameters is not repeated here in the present paper.

3.2. Sound absorption mechanism and its inherent relationship with SBH effects

The space between each pair of rings forms different acoustic cavities. As a rough approximation, the investigated system can be regarded as a series of cavities with varying cavity volume, which are connected in cascade along the structure axial as shown in Fig. 4. For clarity, these cavities are numbered in sequence, starting from the end of the SBH.

Analyses are performed to gain a better understanding of the observed sound absorption. We define the total power dissipation density Δ (SI unit: W/m3) which represents the energy per unit volume dissipated through both the viscous and thermal effects as [24–27]

$$\Delta = \Delta_v + \Delta_t = \boldsymbol{\tau} : \nabla \boldsymbol{u}_1 + \frac{\kappa}{T_0}(\nabla T_1)^2 \tag{7}$$

where $\boldsymbol{\tau}$:∇ $\boldsymbol{u_1}$ is the viscous dissipation function; ":" is the double dot operator (or total inner product); $\boldsymbol{\tau}$ is the viscous stress vector; Δ_v and Δ_t are the viscous and thermal contributions to the dissipation function, respectively. Δ, at different peak frequencies calculated through Eq. (7) [27], is presented in Fig. 5 to quantify the energy dissipation in the system.

Simulation results show that energy dissipation mainly occurs in the areas near the inner edge of the rings. Beyond this small and restricted area, energy dissipation is much weaker and hardly observable. Meanwhile, it is evident that energy dissipation occurs in different areas at different frequencies, with a greater tendency towards the terminating cavities with larger volumes at lower frequencies, and verse versa. For example, the dominant location for energy dissipation at 165 Hz is located around inner edge of the first ring belonging to the first and second cavity, while at 515 Hz, it is the inner edges of the second and third rings belonging to the second and third cavity.

Fig. 6 shows the distribution of sound intensity vector $\boldsymbol{I}$ in the SBH at different absorption peak frequencies, which can be obtained using Eqs. (8) and (9) [27], where * represents the complex conjugation, t is the time and Re represents the real part. $\boldsymbol{I}$ (SI unit: W/m2) is defined as

$$\boldsymbol{I} = \frac{1}{t}\int_0^t p_1 \boldsymbol{u}_1 dt \tag{8}$$

In the frequency domain (assuming harmonic time dependence), one has

$$\boldsymbol{I} = \frac{1}{2} Re(p_1 \boldsymbol{u}_1^{*}) \tag{9}$$

It can be seen that most of the acoustic energy flows in the region near the wall of the inner ring and the region most of the acoustic energy flow in is frequency dependent, more towards the terminating cavities with a larger volume for lower frequencies, and verse versa. These findings are consistent with the above analysis, which further confirms that most of the sound energy is dissipated in the above identified constricted areas, more specifically, near the inner edge of different rings at different excitation frequency.

To further explain the reason why the sound energy is only dissipated in the areas identified above, frequency response analysis of the cascaded cavities in the LSBH is then conducted. The pressure distributions inside the first four cavities at their resonant frequencies are plotted in Fig. 7. It can be seen that pressure variation only occurs near the wall of the inner ring at the resonant frequency, while in other areas the pressure distribution is rather uniform. Knowing that the sound velocity is proportional to the pressure gradient, it is clear that in the above areas, sound velocity is high (as demonstrated in Fig. 8) and the acoustic energy can be effectively dissipated through the interactions between the air and the inner ring wall. This is the reason why a significant portion of the sound energy flows into and gets dissipated in these areas. The cavity volume of these entities exhibits a progressive increase along the axial direction, with the resonance frequency of each cavity contingent upon its specific volume at a given location. In the current scenario, the gradual changes in cavity volume give rise to a continuous modulation of the cavity resonant frequencies. This modulation is characterized by a gradual reduction as one progresses towards the terminus of the LSBH. The frequency response curves from each cavity obtained through FE analysis, plotted in Fig. 9 with corresponding resonance frequencies marked as f_n, clearly demonstrate this. Note f_n is calculated using the nominal and constant sound speed in air, i.e., 340 m/s.

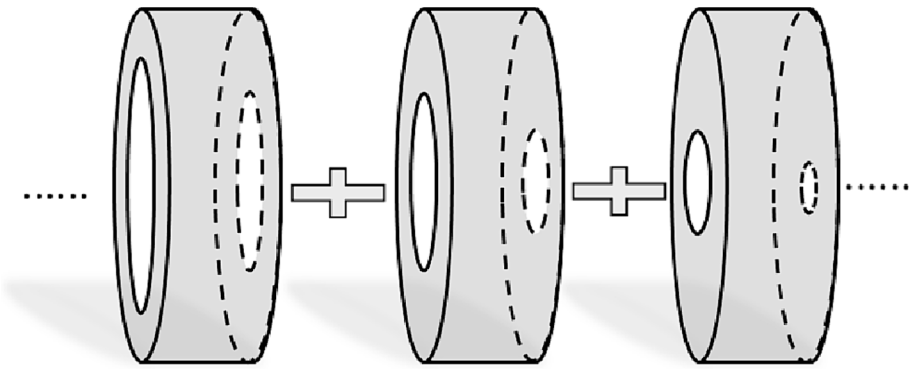

Fig. 4. Cavities formed by adjacent rings in LSBH.

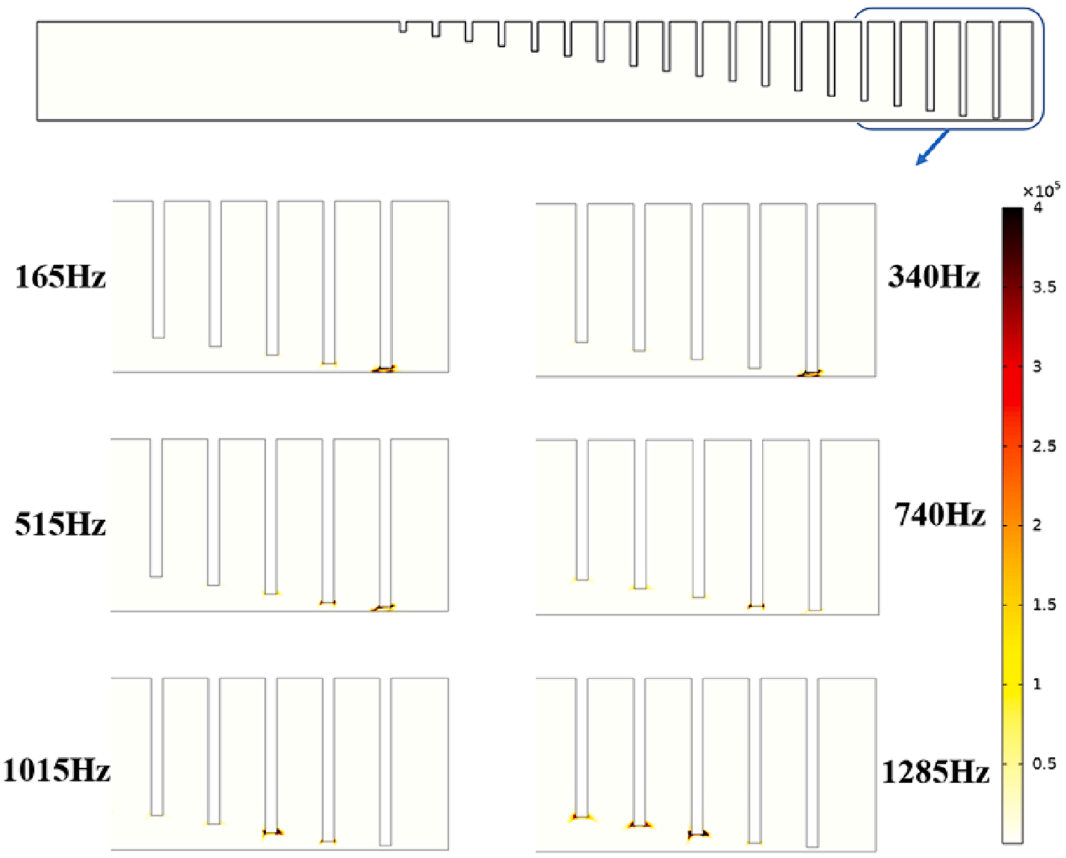

Fig. 5. Total power dissipation density in the SBH end at different sound absorption peak frequencies. The power dissipation density has a unit of mW/m^3.

Fig. 9 shows that although the overlapping of the effective working frequency range of these cascaded resonant cavities could broaden the bandwidth, it cannot ensure such broadband sound absorption since the cavity resonances are not wideband. Moreover, it is noteworthy that this absorption occurs within a frequency range which is way above the effective frequency range shown in Fig. 3, which is conveniently reproduced herein for more in-depth analysis. Indeed, the effective frequency range of these parallel-connected resonance cavities cannot cover the entire effective sound absorption frequency range provided by the designed LSBH absorber in Fig. 3 since the lowest four resonance frequencies of the first four cavities are 270 Hz, 1590 Hz, 1855 Hz, 2145 Hz, respectively, which are not near but much higher than the first four peaks on the absorption curve. It is clear that the estimation of resonance frequency cascade effect using constant sound speed alone cannot explain such low, broadband absorption observed above. These findings highlight the necessity for further incorporating additional considerations for sound energy dissipation mechanism exploration.

To further understand this, the sound pressure distributions inside the duct at different frequencies are plotted in Fig. 10. It is discernible that the acoustic wave undergoes compression within the configured structure, resulting in a reduction of its wavelength. This phenomenon is elucidated by the induced ABH effect, which contributes to the deceleration of sound speed. Consequently, the wavelength of the acoustic wave contracts, leading to wave compression. This compression effect promotes energy localization, notably manifested in the distinct positioning of acoustic energy for varying frequencies. Specifically, at lower frequencies, the acoustic energy tends to localize more towards terminal cavities characterized by larger volumes, thereby creating the phenomenon recognized as the rainbow-trapping effect.

Due to the ABH-induced sound wave slowing-down effect, the effective volume of the resonant cavity is equivalently increased as a result of the reduced sound speed. This leads to the down shifting of the resonance frequencies of each cavity. Consequently, low frequencies with long acoustic wavelengths, initially situated outside the operational frequency range of the sequentially connected cavities, are now within their designated working frequency region. This results in a more advantageous frequency matching with the effective domain of these resonant cavities.

To demonstrate this, transient simulation is conducted to obtain the sound speed variation across the SBH. The time-dependent sound pressure curves of three points in the first cavity shown in Fig. 11 are presented in Fig. 12 to determine the sound speed in the first cavity at 165 Hz, which corresponds to the location of the first absorption coefficient peak value. These three points are equally separated by 5 mm. The sound propagation speed, which is the slop of the curve formed by connecting the projection of the troughs at the three points on the bottom surface in Fig. 12, can be deduced by tracing the position and time arrivals of the first trough at these three points.

From Fig. 12, it can be obtained that the sound propagation speed in the last cavity at 165 Hz is 200 m/s. The sound speeds in other cavities at other acoustic excitation frequencies can also be determined by the same way.

The frequency response curves of cavities considering wave speed reduction at four different peak frequencies, namely, a lowest peak frequency, a highest peak frequency and two randomly selected peak frequencies in between, are plotted in Fig. 13. It can be observed that the resonance frequency of these cavities is down shifted sharply comparing with their respective values presented in Fig. 9 due to the wave speed reduction. The down-shifted values roughly match the locations of cavity resonant frequencies and those of the absorption peaks in Fig. 3. Taking Fig. 13(a) as an example, after considering the slow wave effect, the resonant frequency locations of both cavity 1 and 2 now match well with that of the first absorption peak, suggesting the acoustic energy is dissipated through resonant effects by both cavity 1 and 2. This finding

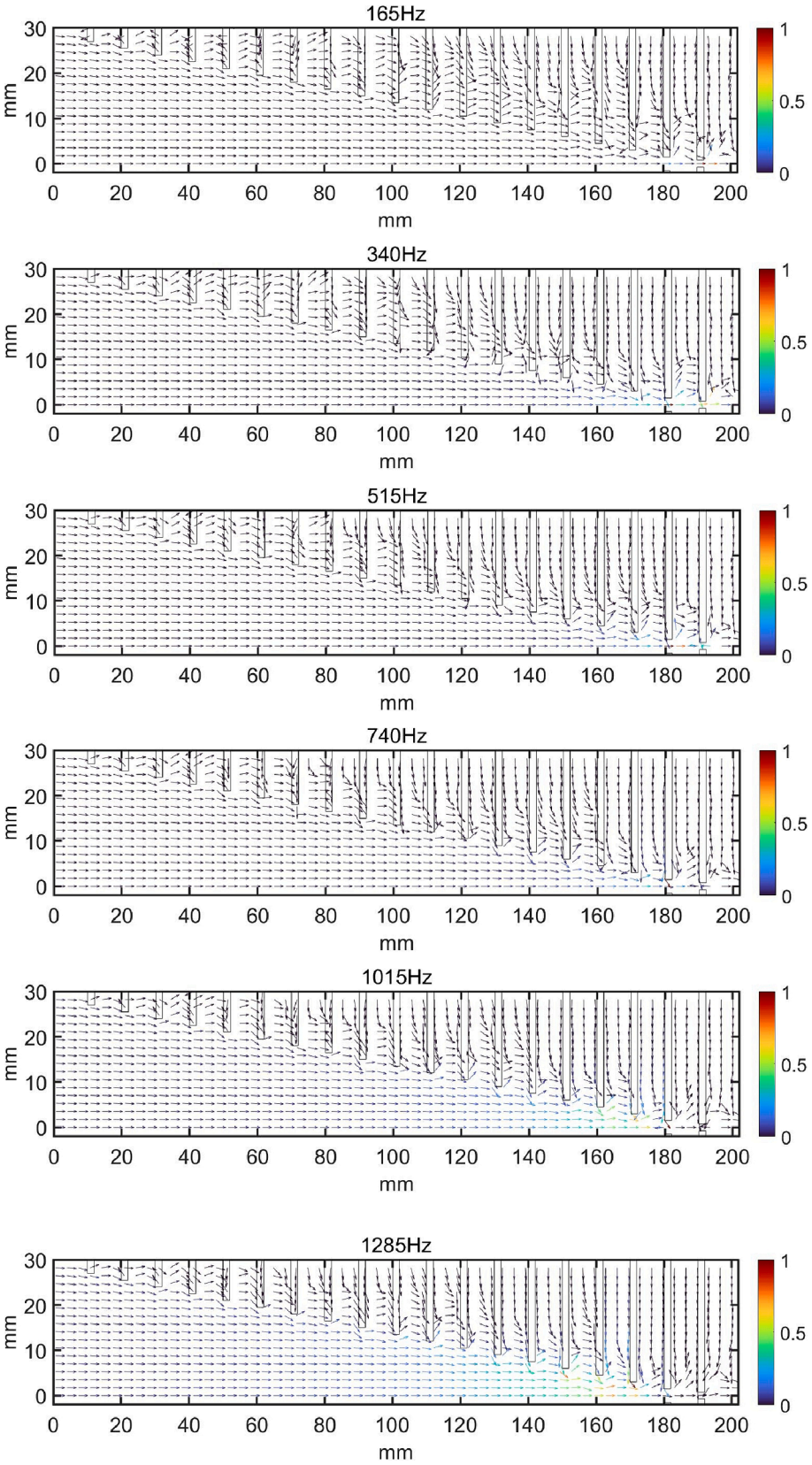

Fig. 6. Sound intensity distribution in SBH at different sound absorption peak frequencies.

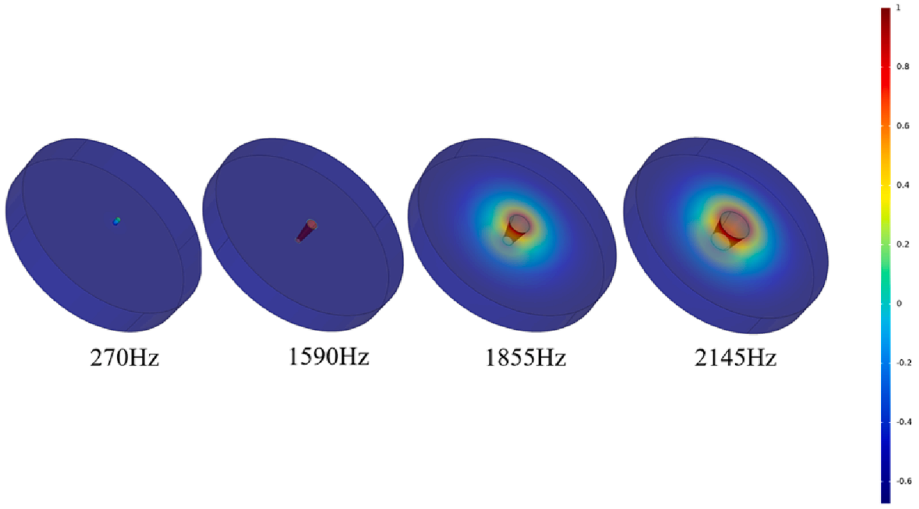

Fig. 7. Sound pressure (unit: Pa) distributions inside the first four cavities at their resonant frequencies using $c_0 = 340$ m/s.

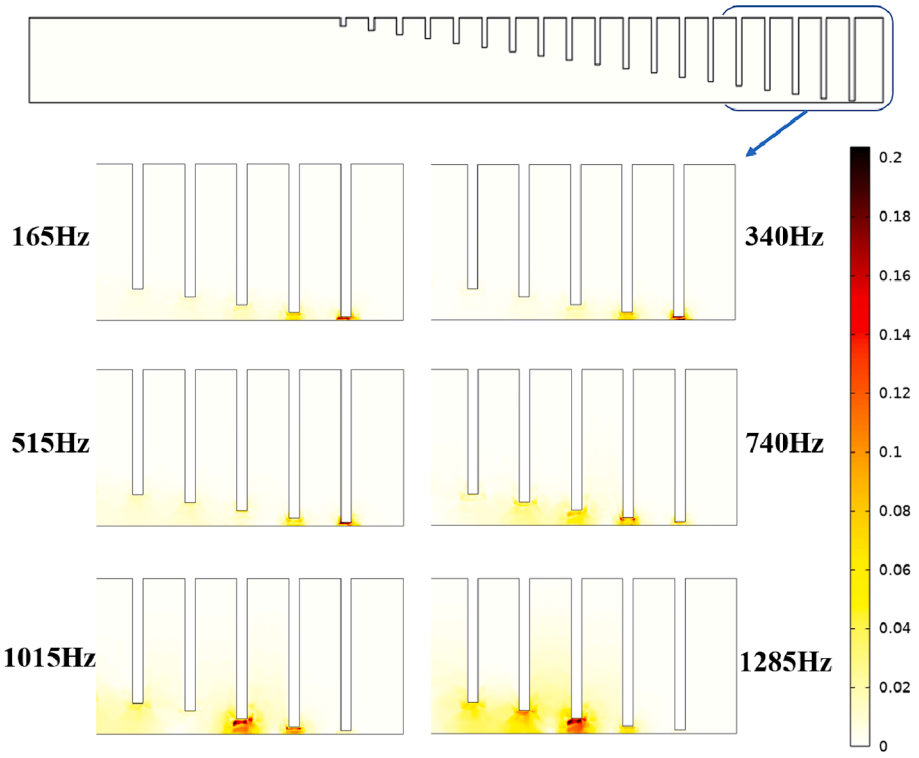

Fig. 8. Instantaneous velocity distribution in SBH at different sound absorption peak frequencies. The local velocity has a unit of *mm*/*ms*.

is consistent with the total power dissipation density analysis shown in Fig. 5 that the acoustic energy at 165 Hz is mainly dissipated in the area around inner edge of the first ring. It is apparent that the appearance of this specific absorption peak is induced by the resonance of different cavities instead of a single one. The same observations also apply to other frequencies shown in Fig. 13(b)-(c). So, the ABH-induced sound wave slowing-down effect and the increase of the effective volume of the resonant cavity is the reason leading to the down shifting of the resonance frequencies of each cavity. Similarly, low frequencies associated with long acoustic wavelengths, initially situated beyond the operational frequency range of the sequentially interconnected cavities, are now encompassed within their operative frequency domain. This results in a more favorable matching with the effective frequency region of these resonant cavities.

It should be stressed from Fig. 13 that individual cavity can exhibit different resonant peaks since the wave retarding level (namely the effective sound speed) is frequency dependent. This leads to a change in the effective depth of the cavity, to vary with respect to the excitation frequency, and consequently an alteration of the resonant frequency of the cavity. This is drastically different from conventional resonators with constant sound speed, which, along with the resonant frequency down-shifting effect, explains the observed broadband behavior of the SBH. For example, the resonant frequency location of cavity 2 can match well with that of three absorption peaks, namely, 165 Hz, 515 Hz and 740 Hz, as shown in Fig. 13 (a), (b) and (c), which is consistent with the results presented in Fig. 5 that the dominant energy dissipation locations at these three frequencies all include the area that around inner edges of the first or second ring belonging to the second cavity. It is apparent that

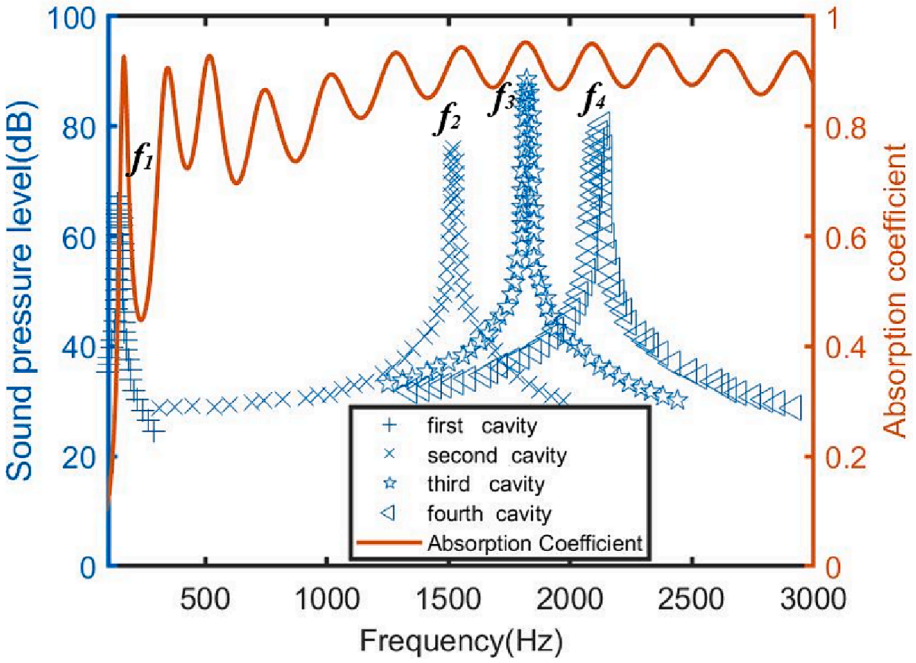

Fig. 9. Sound pressure response for the first four cavities using $c_0 = 340$ m/s along with the calculated sound absorption coefficient curve.

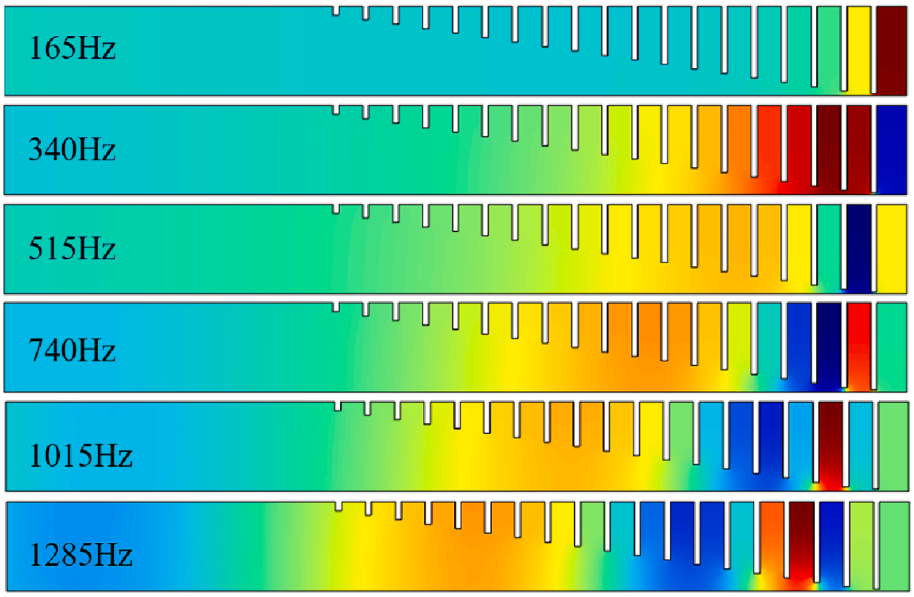

Fig. 10. Sound pressure distributions along the SBH at different sound absorption peak frequencies.

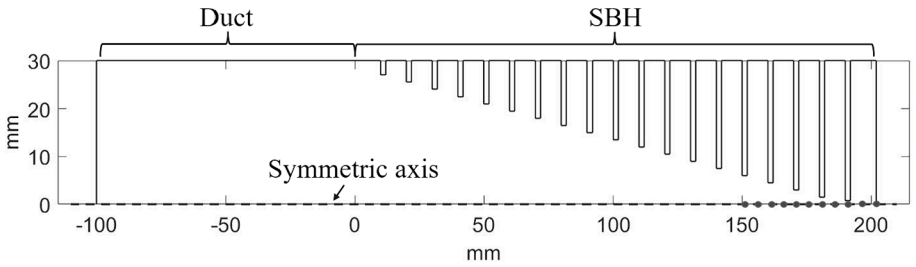

Fig. 11. Locations of points (red points) used for sound speed calculation in LSBH.

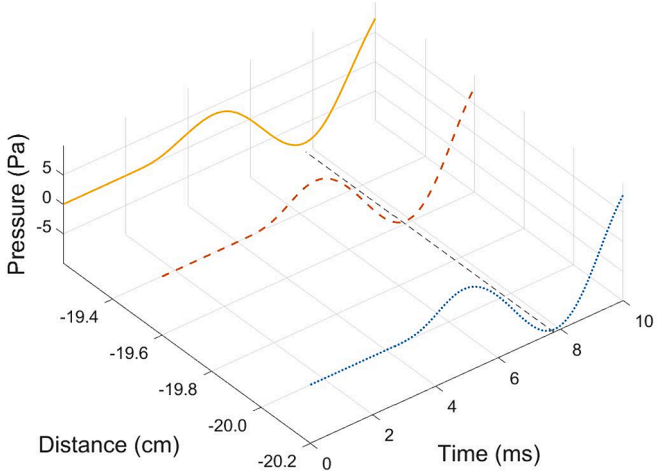

Fig. 12. Time dependent pressure fluctuation curves of three points in the first cavity.

the broadband resonance feature of individual cavity can contribute to the appearance of two or even more absorption peaks and finally effectively broaden the absorption bandwidth as shown in Fig. 13.

Therefore, the low-frequency and broadband sound absorption performance observed above can be attributed to the SBH induced wave retarding effect, its resultant cavity broadband resonance behavior and resonant frequency down-shifting effect together with the cascading resonant cavity effect.

4. Experimental validations

4.1. Sound absorption

Experiments were performed on a LSBH sample using impedance tube measurement to validate the FE model and the predicted sound absorption performance of the designed LSBH device. The geometrical parameters of the manufactured LSBH are the same as the one described in section 2.1.

As shown in Fig. 14 (a), the prototype was manufactured by first dividing the whole structure into several parts: two equally half split circular aluminum alloy duct with several 1.5 mm deep annular grooves scraped out on its inner surface for fixing 19 aluminum alloy rings, whose inner radius decreases following the linear relationship, and one circular plate as the SBH end. All these separate parts were assembled together and then sealed to form the final prototype as shown in Fig. 14 (b).

Fig. 14 (c) shows the test rig for sound absorption measurement, including the impedance tube with installed microphones. The SBH sample was fixed to the end of the tube. Two microphones, separated by a distance of $S = 100$ mm, were flush-mounted on the tube wall, upstream the sample to separate the incident and reflected sound waves in the tube. The selected spacing between the sample and the nearest microphone was 100 mm. White noise was used as excitation. The standard two-microphone transfer function method was employed to obtain the absorption coefficient.

The measured and calculated absorption coefficients are compared in Fig. 15. It can be seen that both the general trend and the magnitude of two curves agree with each other. The salient phenomena predicted by numerical simulations are essentially confirmed, including the sharp increase to near 1 at low frequency around 165 Hz, the oscillation of the curves as well as the broadband feature in sound absorption. Slight discrepancies can mainly be attributed to possible inaccuracy in the air damping estimation, as well as inevitable imperfections in the

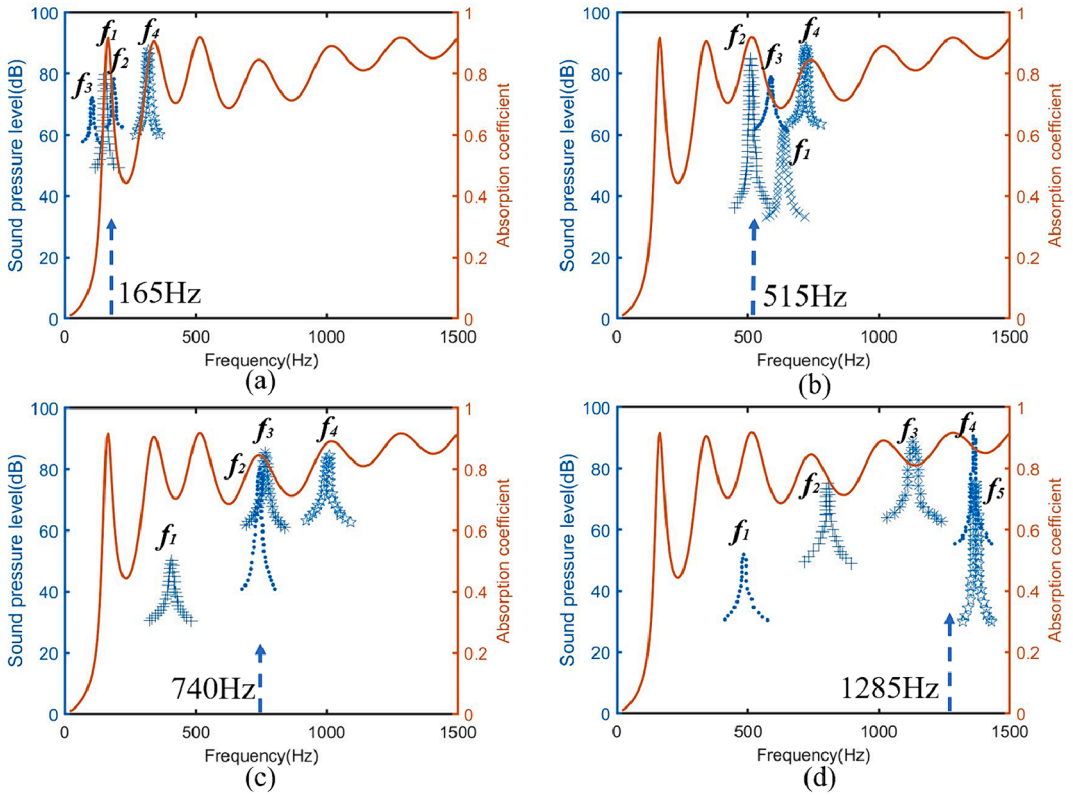

Fig. 13. Sound pressure response of cavities at different sound absorption peak frequencies using slowed sound speed in SBH.

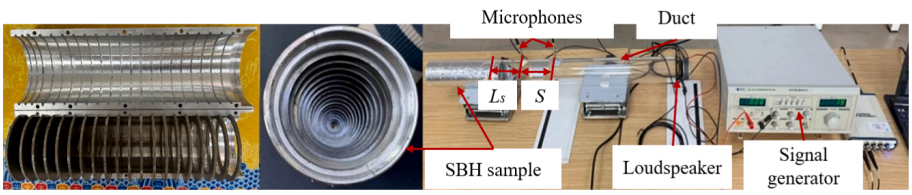

Fig. 14. Photograph of the manufactured LSBH (a) divided parts, (b) assembled prototype and (c) the sound absorption measurement test rig using impedance tube.

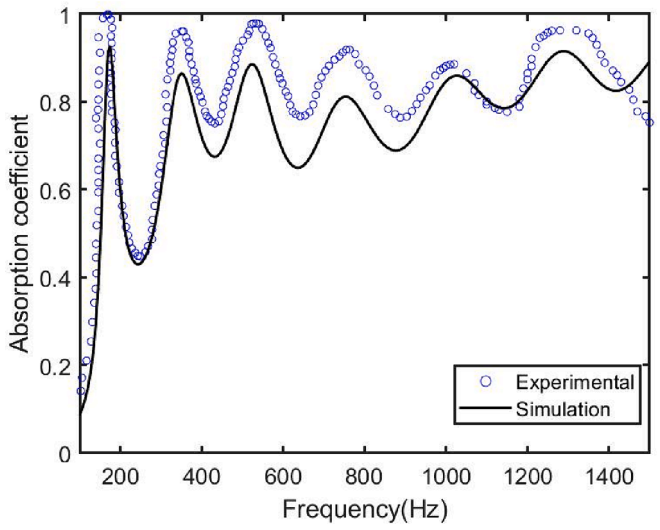

Fig. 15. Comparison between measured absorption coefficient and FE method calculations.

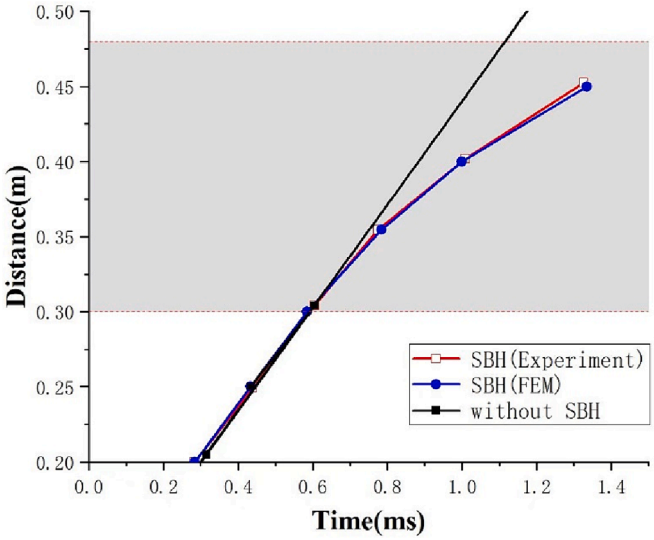

Fig. 16. Comparison of sound wave propagation distance versus time data between transient simulation and experimental data reported in [21]. The shaded area donates the region where sound wave propagates in SBH portion.

manufactured sample and imperfect fitting of the structure to the impedance tube. Nevertheless, the above comparison can verify the FE model prediction and confirm the sound absorption performance of the investigated LSBH device.

4.2. Time domain analysis verification

The validation of the FE transient simulation model employed for the calculation of the sound speed distribution in SBH is also confirmed by experiment. The experimentally measured data in terms of sound wave propagation distance versus time [21] are used for this purpose. The geometrical parameters of the LSBH are same with that reported in Ref. [21]. Fig. 16 clearly show that the simulated results by the FE transient model agree well with the experimental data, with both showing a reduced slope, therefore a reduced sound speed, when acoustic waves enter the SBH section.

5. Conclusions

In summary, we have conducted a comprehensive investigation into the sound absorption mechanism of a discrete SBH structure with a limited number of inner rings. Our findings firstly highlight that viscous and thermal dissipation predominantly take place in the vicinity of the inner edge of the rings, and the primary source of dissipation originates from strong friction occurred in this limited area, as a result of cavity resonance generated high-pressure gradient. Moreover, alongside the wave retarding effect of the SBH, the resonance behavior of cavity, segmented by the ring partitions, differs drastically from that of the conventional narrowband cavity with constant sound speed. Owing to the frequency-dependent slow wave effects of the SBH structure, cavities in the SBH structure show broadband feature with multiple resonant peaks in the frequency range of interest, thus contributing to the multiple absorption peaks and broadened sound absorption. Therefore, the observed SBH low-frequency and broadband absorption performance stems from the synergistic influence of several crucial factors, namely the SBH induced wave regarding effect, its resultant broadband cavity resonance and frequency downshifting effects along with the cascade effect of continuous and spatially varying resonance cavities.

CRediT authorship contribution statement

Xiaoqi Zhang: Writing – review & editing, Writing – original draft, Validation, Methodology, Formal analysis. **Nianwen He:** Writing – review & editing, Writing – original draft, Validation, Methodology, Formal analysis. **Li Cheng:** Supervision. **Xiang Yu:** Supervision, Writing – review & editing. **Linke Zhang:** Resources. **Fucai Hu:** Resources.

Declaration of competing interest

The authors declare that they have no known competing financial interests or personal relationships that could have appeared to influence the work reported in this paper.

Data availability

Data will be made available on request.

Acknowledgements

The research reported here was supported by Natural Science Foundation of Hubei Province, China (Grant No. 2022CFB847). LC and XY acknowledge the financial support from the Research Grants Council of Hong Kong under Grant No. PolyU 15201822

References

[1] Mironov M. Propagation of a flexural wave in a plate whose thickness decreases smoothly to zero in a finite interval. Sov Phys Acoust 1988;34:318–9.
[2] Krylov VV, Tilman F. Acoustic 'black holes' for flexural waves as effective vibration dampers. J Sound Vib 2004;274:605–19.
[3] Krylov VV. New type of vibration dampers utilising the effect of acoustic 'black holes'. Acta Acustica United Acustica 2004;90(5):830–7.
[4] Einstein A, Sitzungsber K. Preuss Akad Wiss 1916;1:688.
[5] Ma L, Zhang S, Cheng L. A 2D daubechies wavelet model on the vibration of rectangular plates containing strip indentations with a parabolic thickness profile. J Sound Vib 2018;429:130–46.
[6] Deng J, Zheng L, Guasch O, Wu H, Zeng P, Zuo Y. Gaussian expansion for the vibration analysis of plates with multiple acoustic black holes indentations. Mech Syst Sig Process 2019;131:317–34.
[7] Zhou T, Chazot JD, Perrey-Debain E, Cheng L. Partition of Unity finite element method for the modelling of acoustic black hole wedges. J Sound Vib 2020;475:115266.
[8] Tang L, Cheng L, Ji HL, Qiu JH. Characterization of acoustic black hole effect using a one-dimensional fully-coupled and wavelet-decomposed semi-analytical model. J Sound Vib 2016;374:172–84.
[9] Mironov M, Pislyakov V. One-dimensional acoustic waves in retarding structures with propagation velocity tending to zero. Acoust Phys 2002;48:347–52.
[10] Mironov M, Pislyakov V. One-dimensional sonic black holes: exact analytical solution and experiments. J Sound Vib 2020;473:115223.
[11] EI-Ouahabi A, Krylov VV, O'Boy D. Investigation of the acoustic black hole termination for sound waves propagating in cylindrical waveguides, in: Proceedings of the Inter-noise and Noise-con Congress and Conference, San Francisco, USA, Institute of Noise Control Engineering, 2015.
[12] EI-Ouahabi A, Krylove VV, O'Boy D. Experimental investigation of the acoustic black hole for sound absorption in air, in: Proceedings of 22nd International Congress on Sound and Vibration, Florence, Italy, 2015.
[13] Guasch O, Arnela M, Sanchez-Martín P. Transfer matrices to characterize linear and quadratic acoustic black holes in duct terminations. J Sound Vib 2017;395:65–79.
[14] Guasch O, Sanchez-Martín P, Ghilardi D. Application of the transfer matrix approximation for wave propagation in a metafluid representing an acoustic black hole duct termination. Appl Math Model 2020;77:1881–93.
[15] Hollkamp JP, Semperlotti F. Application of fractional order operators to the simulation of ducts with acoustic black hole terminations. J Sound Vib 2021;465:115035.
[16] Mi Y, Zhai W, Cheng L, Xi C, Yu X. Wave trapping by acoustic black hole: simultaneous reduction of sound reflection and transmission. Appl Phys Lett 2021;118:114101.
[17] Umnova O, Brooke D, Leclaire P, Dupont T. Multiple resonances in lossy acoustic black holes - theory and experiment. J Sound Vib 2023;543:117377.
[18] Mousavi A, Berggren M, Wadbro E. How the waveguide acoustic black hole works: a study of possible damping mechanisms. J Acoust Soc Am 2022;151:4279–90.
[19] Cervenka M, Bednarik M. On the role of resonance and thermoviscous losses in an implementation of "acoustic black hole" for sound absorption in air. Wave Motion 2022;114:103039.
[20] Zhang X, Cheng L. Broadband and low frequency sound absorption by sonic black holes with micro-perforated boundaries. J Sound Vib 2021;512:116401.
[21] Li S, Xia J, Yu X, Zhang X, Cheng L. A sonic black hole structure with perforated boundary for slow wave generation. J Sound Vib 2023;559:117781.
[22] Hunt FV. Notes on the exact equations governing the propagation of sound in fluids. J Acoust Am 1955;27:1019–39.
[23] Kinsler LE, Frey AR, Coppens AB, et al. Fundamentals of acoustics[M]. John wiley & sons; 2000.
[24] Tang Y, Ren S, Meng H, Xin F, Huang L, Chen T, et al. Hybrid acoustic metamaterial as super absorber for broadband low-frequency sound. Sci Rep 2017;7:43340.
[25] Duan M, Yu C, Xu Z, Xin F, Lu T. Acoustic impedance regulation of helmholtz resonators for perfect sound absorption via roughened embedded necks. Appl Phys Lett 2020;117:151904.
[26] Duan M, Yu C, Xin F, Lu T. Tunable underwater acoustic metamaterials via quasi-helmholtz resonance: from low-frequency to ultra-broadband. Appl Phys Lett 2021;118:071904.
[27] Multiphysics C. Acoustics Module User's Guide. 2022.